

Evolution of the passive and active microwave signatures of a large sea ice feature during its $2\frac{1}{2}$ -year drift through the Arctic Ocean

Francis Gohin, Alain Cavanié, and Robert Ezraty

Institut Français de Recherche pour l'Exploitation de la Mer, Brest, France

Abstract. Although estimation of the total ice concentration from special sensor microwave imagers (SSM/I) has proven to be successful, none of the various algorithms developed to discriminate new and older ice provide satisfying results. While the strong contrast between the emissivity of sea ice and that of open water can be utilized to provide reliable estimators of the total ice concentration, passive microwave characteristics of second-year and multiyear ice may locally evolve in different ways, even during the cold season. Scatterometers, as the active microwave instrument in wind mode (AMI-wind) on board the European Remote Sensing Satellites (ERS), provide backscatter data which have a higher sensitivity to the surface topography of ice and a better stability in time, at a resolution compatible with the SSM/I measurements. Here we present the evolutions of the microwave properties of an ice feature appearing along the shores of Novosibirskiy Ostrova (New Siberian Islands) at the end of July 1992 as the ice ages during its 3-year drift toward the Fram Strait. The track of this well-defined ice surface is easily followed on the maps of the backscatter coefficient provided by the AMI-wind during the cold season. In summer, because of melting, the ice undergoes critical changes which alter its microwave signatures and hamper automatic tracking. Moreover, on approaching the Fram Strait the resolution of the scatterometer is not sufficient to capture the complex and rapid transformations of the ice cover. To compensate for this, buoy data obtained from the International Arctic Buoy Program are used, alone during summers or together with satellite data, to build basin-wide ice displacement fields. These displacement fields, successively applied to each pixel of the ice feature selected, provide a series of Lagrangian observations. During the drift, which ends in May 1995, the active and passive signatures evolve coherently, except for the cold season 1992–1993 when unrealistic multiyear ice concentrations are deduced from the brightness temperatures, which, at that time, are much less stable than the backscatter coefficient over the ice surface tracked, identified as second-year ice.

1. Introduction

The concentration and the type distribution of sea ice can be considered as results of the global climate and statistically analyzed as indicators of its fluctuations [Gloersen, 1995] or presented as major elements of the world hydroclimatic system, since the export of fresh water and ice through the Fram Strait influences convection and deep water formation. The origin of the so-called Great Salinity Anomaly [Dickson *et al.*, 1988] has been attributed to an increase in sea ice extent at the end of the 1960s [Aagaard and Carmack, 1989]. On the basis of results of a simulation of the Arctic ice-ocean system for 1955–1975, Häkkinen [1993] attributes the widening of the transpolar drift stream in 1968 to a well-developed low-pressure area extending from the Iceland Sea to the Barents and Kara Seas opposed to the Beaufort High, which recovers after several years of weakening. This effect being amplified by advection of thicker ice north of Greenland, the author evaluates to 1600 km^3 the excess of fresh water exported through the Fram Strait that year, leading to a total export about twice as large as the average.

Copyright 1998 by the American Geophysical Union.

Paper number 97JC03333.
0148-0227/98/97JC-03333\$09.00

Considering that the sensible heat flux from the ocean to the atmosphere is 1 or 2 orders of magnitude greater over thin ice than over thick multiyear ice, the determination of the ice type is crucial for Arctic climate models. The special multichannel microwave radiometer on board Nimbus 7, launched in 1978, and its successor, the special sensor microwave imager (SSM/I) in 1987, have provided a long temporal record of data. These instruments offer a daily coverage over polar oceans with a fairly coarse resolution (30–50 km). Multichannel algorithms have been developed to estimate total sea ice concentration and the concentration of multiyear ice [Steffen *et al.*, 1992]. Estimating ice thickness from space is much more difficult, though local thresholding methods can be used to separate sea ice types representing thickness categories on images provided by synthetic aperture radars (SAR) [Haverkamp *et al.*, 1995]. However, sufficient sets of data over the whole Arctic Ocean are crucially missing, even if we agree that our understanding of the Arctic climate will depend more and more on modeling, guided by data assimilation. Walsh and Zwally [1990] consider that so many points have to be assessed in models and products derived from the observations that these two possible approaches to quantify the ice pack on the basis of numerical modeling or observations have still to be compared with each other and improved.

Although they are designed to measure winds at the ocean surface, scatterometers provide valuable information over sea ice with a resolution similar to that of the SSM/I. The active microwave instruments in wind mode (AMI-wind) flown aboard the European Remote Sensing Satellites (ERS) are C band (5.3 GHz), vertically (VV)-polarized scatterometers. AMI-wind data have been provided by ERS-1 from August 1991 to June 1996 and since then by ERS-2. Because the AMI-wind backscatter over sea ice is independent of the azimuth angle but varies as a function of incidence angle, maps of the backscatter coefficient at a fixed incidence angle of 40° [Gohin and Cavanié, 1994] have been produced and distributed by the Centre ERS d'Archivage et de Traitement (CERSAT) after projection on the same polar grid used by the National Snow and Ice Data Center (NSIDC) to present SSM/I data. Backscatter data can thus be conveniently compared to the brightness temperatures as well as to the derived products of the SSM/I (ice concentration and ice type).

In this study the variability of ice parameters retrieved from low-resolution microwave instruments is investigated by following the evolution, with time, of the microwave signatures of a large ice feature drifting toward the Fram Strait. Over the area studied, which was almost fully ice covered, the multiyear ice concentration is of particular importance. As noted by several authors [Comiso, 1986, 1990; Thomas, 1993; Kwok *et al.*, 1996], this multiyear ice concentration as obtained from SSM/I fluctuates during the cold season and is low compared to the ice concentration estimated at the end of the previous summer.

The present Lagrangian approach enlarges a concept already presented by Kwok *et al.* [1995], who proposed to determine the age distribution of sea ice from Lagrangian observations of ice displacements estimated from SAR data; they selected a timescale in days and a 5-km pixel size. Our study is based on a timescale of months and a pixel size of 25 km, which are adapted to the size of the Arctic Ocean, the mean residence time of sea ice from its formation to its evacuation, and the size of the selected ice feature. This feature, which covers about 400,000 km², is followed from its initial formation (as ice surviving its first summer) along the northern shores of Novosibirskiye Ostrova (New Siberian Islands) at the end of July 1992 until its evacuation through the Fram Strait in May 1995.

Eulerian fields of ice displacement, for 8-week periods, are calculated over the Arctic Ocean by a two-step procedure using both backscatter maps and buoy data from the International Arctic Buoy Program (IABP). By applying the successive displacement fields to each pixel of the selected ice feature a Lagrangian series of microwave observations is produced. This 2½-year time series sets in evidence the seasonal and interannual fluctuations of the active (AMI-wind) and passive (SSM/I) microwave signatures of ice as it progresses through the Arctic Ocean and ages, evolving from the state of essentially second-year ice to that of third- and fourth-year ice. Thus variations in active and passive microwave signatures are observed without any significant perturbation caused by ice advection.

2. Data

2.1. Buoy Data

The buoy data have been obtained from the Polar Science Center at the University of Washington. The data set contains daily positions in latitude and longitude as well as the identi-

fication code of the buoys. These positions have been transformed in horizontal and vertical coordinates (respectively columns and rows) on the 25- × 25-km resolution, 304- × 448-pixel grid of the stereopolar projection used at NSIDC [Gloersen *et al.*, 1992].

At the start day of this study (December 3, 1992), 45 buoys were deployed over the area selected for ice tracking (Plate 1). In March 1993, 11 buoys were added to the network, with an important concentration north of Novosibirskiye Ostrova, around the ice feature to be tracked. As about one tenth of the buoy positions are missing on a daily basis, the number of buoy displacements, calculated using pairs of individual positions 8 weeks apart, is reduced to <40.

2.2. Satellite Data

2.2.1. AMI-wind backscatter data. The AMI-wind has three antennas pointing 45°, 90°, and 135° to the right of the satellite ground track. Thus, because the satellite is yaw steered, the fore and aft beams point to the surface with the same incidence angles. The antenna swaths are composed of 19 cells, 25 by 25 km in size, starting 225 km from the ground track. Given a nominal flight altitude of 800 km, the incidence angles of the electromagnetic beams vary approximately from 25° to 59° for the fore and aft beam and from 18° to 45° for the central beam. The noise level of the individual backscatter measurements is about 6% and is almost constant over the whole range of incidence angles and backscatter values, σ^0 .

Over consolidated sea ice, within the range of incidence angle (θ) of the AMI-wind, σ^0 (in decibels) is well described by a linear function of θ , the slope depending on sea ice type [Gohin and Cavanié, 1994]. A similar behavior was observed by Drinkwater and Carsey [1991] over the Antarctic Ocean for Seasat A scatterometer system (SASS) at Ku band. This property is used to map backscatter values at the constant incidence angle of 40° (σ_{40}^0) over the whole polar ocean. Because of the grid size, of the ERS orbiting cycle (3-, 35-, or 135-day repeat cycle), of the 500-km swath of the AMI-wind, and of interruptions due to SAR imaging mode, it proved necessary to use 1 week of data in order to cover the whole polar ocean and obtain a reasonable stability of the final map. The following procedure is used: for each cell of the polar grid an estimation of $d\sigma/d\theta$ is performed using, on the one hand, the σ^0 at the incidence angle of the central antenna and, on the other hand, the average of the σ^0 of the fore and aft beams. For each pixel and over the whole week a mean slope $d\sigma/d\theta$ is estimated, and by applying the linear equation (1), σ_{40}^0 are calculated and averaged.

$$\sigma_{40}^0 = \sigma_{\theta}^0 + \frac{d\sigma}{d\theta} (40 - \theta) \quad (1)$$

During the cold seasons, using two consecutive maps and assuming that, over selected areas and pixel by pixel, the differences of σ_{40}^0 are only due to measurement and processing noise, it is possible to estimate the quality of the final image as the square root of half the variance of the relative differences. Such a computation indicates that the relative noise decreases from 8 to 2% when σ_{40}^0 increases from 0.0025 to 0.15. In the following, only σ_{40}^0 values will be used, thus the subscript "40" will be dropped in the notation.

Plate 1 presents a time series of σ^0 maps, from December 1992 to May 1995, on which are plotted the IABP buoy positions. During the summer periods, because of surface melt and

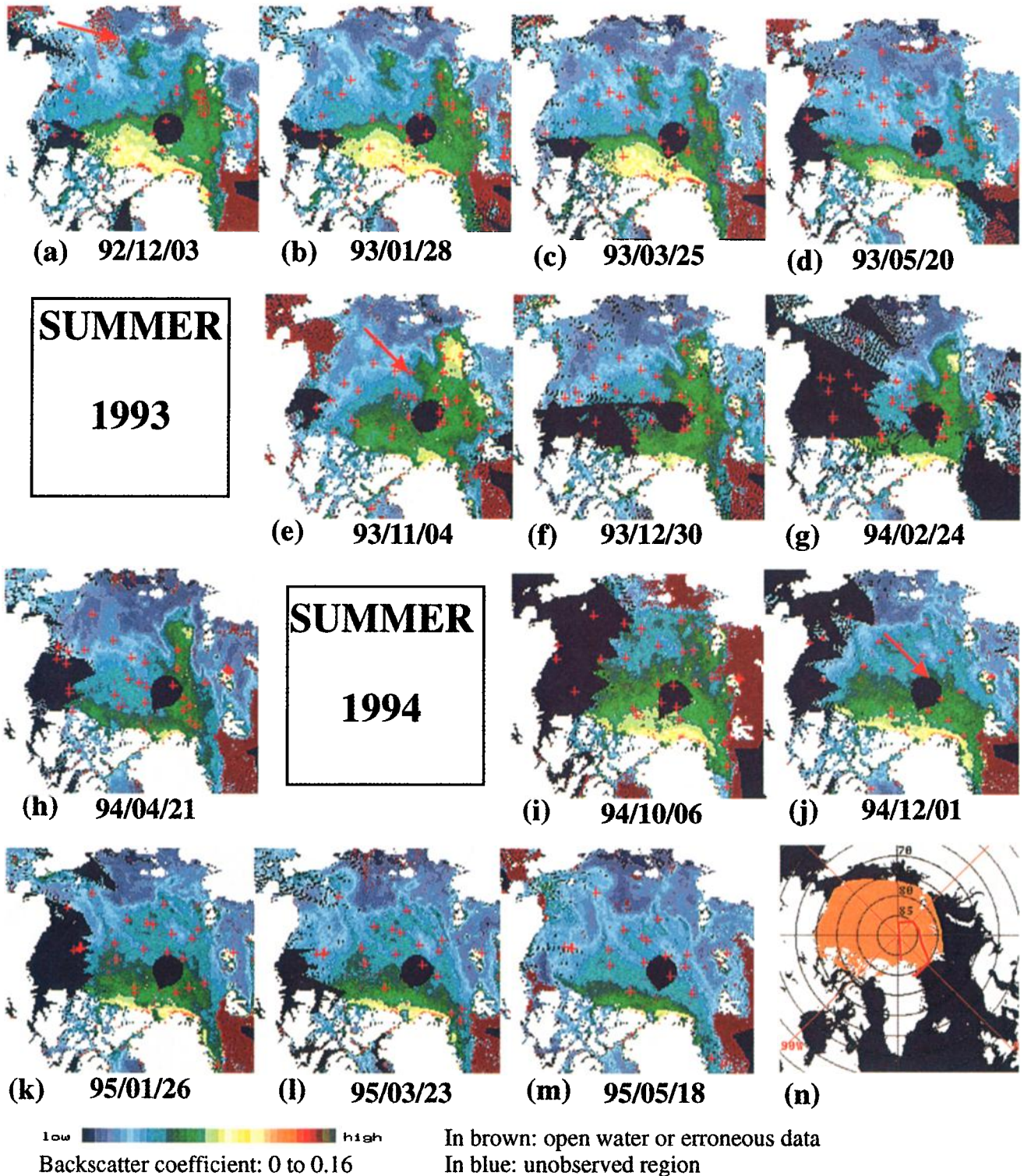


Plate 1. Weekly active microwave instrument in wind mode (AMI-wind) backscatter maps spanning the drift of the selected ice feature. Three arrows show its positions after the summers of 1992, 1993, and 1994. Images are separated by 8-week periods centered on the indicated dates. Red crosses indicate buoy positions. Plate 1n shows the area where displacements are calculated and the limit of the Fram Strait area, in red.

ponds, backscatter signatures deviate so much from those of winter sea ice that they are useless for tracking; therefore corresponding maps were skipped. Although year to year backscatter variations are evident, for example, north of Greenland, the annual signatures remain stable throughout the winter

periods with some indication of surface changes in late April or May. The stability of σ^0 allows us to identify the sea ice structure, marked by an arrow, on the December 1992 map and to follow it, visually, during its 1992–1993 winter drift until summer melt blurs the map.

2.2.2. SSM/I data. The SSM/I measures microwave emission at 19.35, 37.0, and 85.5 GHz in both vertical and horizontal polarizations and at 22.23 GHz in vertical polarization only. The footprint sizes are 55, 32, 13, and 49 km, respectively. The incidence angle is constant and equal to 53°.

The data used here are the daily Defense Meteorological Satellite Program (DMSP) F11 brightness temperature grids at 19 GHz (vertical and horizontal polarization) and 37 GHz (vertical polarization) provided by the NSIDC. These temperatures (T_b) are combined to compute the gradient and polarization ratios (GR and PR) defined as $GR = (T_{b_{37v}} - T_{b_{19v}})/(T_{b_{37v}} + T_{b_{19v}})$ and $PR = (T_{b_{19v}} - T_{b_{19h}})/(T_{b_{19v}} + T_{b_{19h}})$. These ratios damp surface temperature changes and are used as variables to characterize ice types and to estimate first-year, multiyear, and total ice concentration (C_{FY} , C_{MY} , C_T) according to the NASA team algorithm [Cavalieri, 1992]

$$C_{FY} = (a_0 + a_1PR + a_2GR + a_3PRGR)/D \quad (2)$$

$$C_{MY} = (b_0 + b_1PR + b_2GR + b_3PRGR)/D \quad (3)$$

$$C_T = C_{FY} + C_{MY} \quad (4)$$

where

$$D = c_0 + c_1PR + c_2GR + c_3PRGR \quad (5)$$

The coefficients a_i , b_i , and c_i are derived from constant brightness temperature of tie points corresponding to open water, first-year, and multiyear ice for the Arctic or open water, type A and type B ice for the Antarctic.

3. Estimation of Basin-Wide Ice Displacement Fields

3.1. General Presentation of the Two-Step Method

The method developed to build ice displacement fields is based on a two-step procedure somewhat similar to that employed by Fily and Rothrock [1987], adapted to our low-resolution satellite data. Fily and Rothrock track sea ice by a nested correlation method applied to Seasat SAR images. From highly smoothed images they calculate a first-guess displacement field, used to guide the search for maximum correlation between small areas of ice common to two successive high-resolution images. Here first-guess displacements are calculated on the NSIDC grid for one pixel out of four along both horizontal and vertical axes (100- × 100-km coarse grid). The horizontal and vertical displacements are obtained from IABP buoy displacements by an objective interpolation method, kriging [Olea, 1974]. For each displacement on the coarse grid, kriging yields an estimation of the local error. A detailed description of kriging is presented in section 3.2.

The second step of the procedure takes advantage of the stability of σ^0 in time. Ice located at point X (Plate 2e–2f) is supposed to have drifted to a new position located within a circle whose radius is proportional to the error estimation. The center of the circle, X_0 , corresponds to the initial position shifted by the first-guess displacement. On the fine grid, all 7- × 7-pixel arrays of the backscatter image 8 weeks later, whose center pixels fall within the circle, are searched to find the one that has the maximum correlation with the 7 × 7 array centered on X on the initial image. When a highly correlated array is found, the center of this array defines a new tie point X' associated to X. Limiting the search to circular areas con-

strained by the error estimations provided by the kriging procedure gives the tracking algorithm the required restriction for search (unlimited areas would lead to many fliers); for points in the vicinity of buoys the first-guess displacement will not be modified since the radius of the circle will be small due to the reduced error estimate. Details of this search procedure, applied automatically on every point of the coarse grid, are given in section 3.4. By kriging, a new estimation of the displacement field over the coarse grid can now be made using both buoy and backscatter image displacements. Finally, over the Arctic area selected (colored in orange on Plate 1n), a bilinear interpolation is applied to extend the displacement fields over the fine NSIDC grid.

The improvement due to the second step will not be uniform on the grid, as some areas have been deliberately excluded (the Fram Strait area within the red box, on Plate 1n) or are deprived of AMI-wind observations because of SAR operation (part of the Beaufort Sea on Plate 1g). The method will be most efficient in places where ice is strongly featured; such conditions are found around the ice feature originating from north of Novosibirskiye Ostrova, particularly during the 1992–1993 cold season.

3.2. Kriging Hypotheses

Considering the random variable $D(x)$, where D is the displacement along the X or Y axis, we have to set a minimum number of hypotheses that are necessary to obtain the estimations of D . Elementary hypotheses in geostatistics [Matheron, 1970] do not deal with the mean value of $D(x)$ at any location x , as the mean is unknown and different from one location to another, but deal with the increments $[D(x+h) - D(x)]$ of the random variable D between two locations x and $x+h$. They are formulated as

$$\mathcal{E}[D(x+h) - D(x)] = 0 \quad (6)$$

$$V(h) = \frac{1}{2} \mathcal{E}\{[D(x+h) - D(x)]^2\} \quad (7)$$

where \mathcal{E} is the expected value and V is the semivariogram. Equation (6) states that there is no trend in the increments of the displacement, and (7) states that their variance depends only on the distance, h , between their locations and not on their specific locations.

The semivariograms of the displacements along the X and Y axes have been modeled using the so-called spherical model [Curran, 1988].

$$V(h) = S[1.5(h/a) - 0.5(h/a)^3] \quad h \leq a \quad (8)$$

$$V(h) = S \quad h > a \quad (9)$$

where S and a are defined as the sill and the range, respectively.

Figure 1 shows the adjustment of parameters S and a to the experimental semivariograms. For both components of the displacement a unique range has been estimated equal to 100 pixels (2500 km). However, the X and Y displacement sills are very different, 20 and 45 square pixels, respectively. The higher sill observed for the Y component can be explained by its strong gradient north of the Fram Strait. As ice approaches the Strait, it moves slowly horizontally while it accelerates along the Y axis.

3.3. Estimating the Displacement by Kriging

For each point of the coarse grid over the selected Arctic ocean area the ice displacement is estimated by local kriging

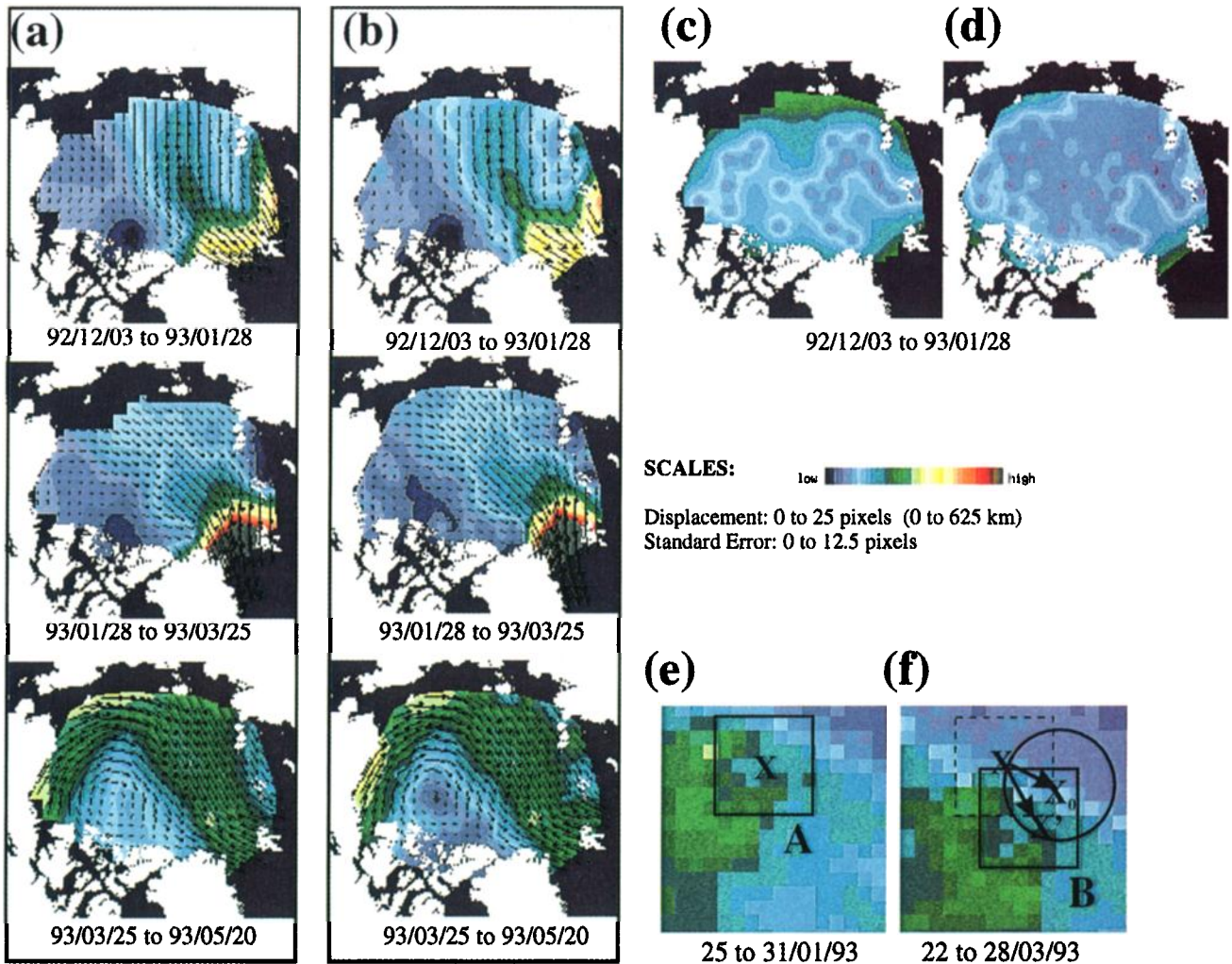


Plate 2. Ice motion estimated for the three initial periods of the study (a) from buoys alone and (b) from buoys and images. Standard error of the ice drift for the first period is presented (c) for buoys only and (d) for buoys and images. (e, f) The method to modify the initial displacement field calculated from the buoy displacements alone is illustrated. X is a location on the coarse grid to which is associated, by kriging of buoy data, position X_0 . This first-guess position is improved by searching for the 7×7 -pixel array B most correlated to the array A centered on X.

using the six closest displacements. The kriging estimator, $D^*(x)$, is a linear combination of $D(x_i)$

$$D^*(x) = \sum_{i=1,6} \lambda_i D(x_i) \quad (10)$$

The λ_i result from the minimization of the variance of errors, $\mathcal{E}\{[D^*(x) - D(x)]^2\}$, under the condition of no bias, $\mathcal{E}[D^*(x) - D(x)] = 0$. The latter condition is satisfied by choosing the weights, λ_i , such that their sum is equal to one. Then from (6)

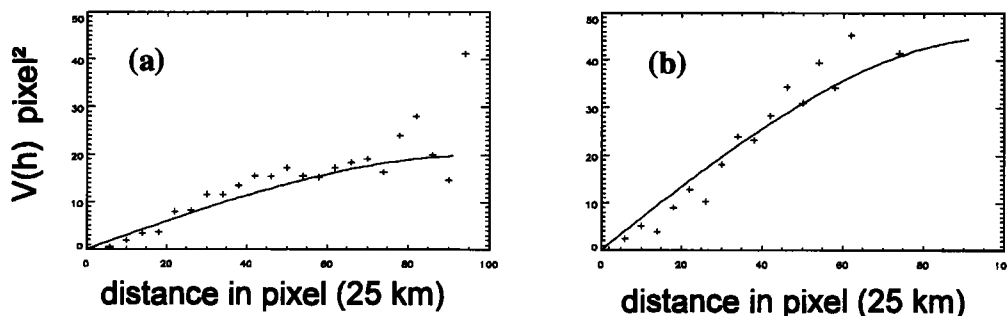


Figure 1. Semivariograms of ice displacements for 8-week periods along the (a) X and (b) Y axis of the National Snow and Ice Data Center (NSIDC) polar grid.

$$\begin{aligned} \mathcal{E}[D^*(x) - D(x)] &= \mathcal{E}\left[\sum_{i=1,6} \lambda_i D(x_i) - D(x)\right] \\ &= \sum_{i=1,6} \lambda_i \mathcal{E}[D(x_i) - D(x)] = 0 \end{aligned} \quad (11)$$

From (7) and the constraint on the sum of the λ_i , the following equation results [Matheron, 1970]

$$\begin{aligned} \mathcal{E}\{[D^*(x) - D(x)]^2\} &= \sum_{i=1,6} \lambda_i \mathcal{V}[h(x_i, x)] \\ &\quad - \sum_{i=1,6} \sum_{j=1,6} \lambda_i \lambda_j \mathcal{V}[h(x_i, x_j)] \end{aligned} \quad (12)$$

The minimization of $\mathcal{E}\{[D^*(x) - D(x)]^2\}$ leads to a set of equations linear in λ_i , which, after inversion, yields unique λ_i solutions.

3.4. Extracting Displacement From Successive Backscatter Images

In order to improve the displacement field estimated from buoy data alone, displacements are also deduced from successive backscatter images and incorporated in the set of second-step displacements. Each pixel on the coarse grid is now considered as the center of a 7×7 -pixel array on the fine grid.

For a pair of 7×7 pixel arrays, A on the initial image and B on the following image, the correlation $C_{a,b}$ is defined as

$$C_{a,b} = \frac{\sum_{i=1,n} \sigma_{a,i}^0 \sigma_{b,i}^0 - n \overline{\sigma_a^0} \overline{\sigma_b^0}}{\sqrt{\sum_{i=1,n} (\sigma_{a,i}^0 - \overline{\sigma_a^0})^2 \sum_{i=1,n} (\sigma_{b,i}^0 - \overline{\sigma_b^0})^2}} \quad (13)$$

where $\overline{\sigma_a^0}$ and $\overline{\sigma_b^0}$ are the means of the arrays A and B and n is the number of validated pairs ($\sigma_{a,i}^0, \sigma_{b,i}^0$) extracted from the arrays. Each pair ($\sigma_{a,i}^0, \sigma_{b,i}^0$) is validated if both backscatter data have not been recognized as land, open water, or spurious observations (such cases occur during the AMI-wind/SAR switches). If n , the maximum value of which is equal to 49, is lower than 41, the displacement is not validated.

If the correlation between array A and array B is >0.75 , the initial displacement is kept unchanged. If not, the algorithm seeks the maximum correlation at successive distances increasing either from one to six pixels or twice the standard error of kriging, the smaller of the two being chosen; the standard error of kriging is defined as the square root of the sum of the error variances along the horizontal and vertical axes. When a correlation >0.75 is found, the search for maximum correlation does not extend beyond that distance; the displacement is validated and added to the set of buoy displacements. The displacement is not validated if the correlation coefficient does not reach a value of 0.75. These additional displacements, with an error variance set to 8 square pixels, are then used for kriging. This value of the error variance gives them little weight when buoy data are present in their vicinity.

The performance of the algorithm is linked to the evolution of the correlation, $C(d)$, as the lag, d , increases from 0 to 5 pixels. For A centered on a buoy position and B centered on the position of the same buoy, 8 weeks later, the correlation coefficient, noted $C(0)$, would be equal to 1 if σ^0 were perfectly stable and if ice were rigid, without convergence or divergence. Shifting B by a distance d (in pixels) in any direction around the true position of the buoy, the corresponding

correlation coefficient between A and B will decrease from $C(0)$ to $C(d)$. The results of such a numerical experiment applied to the pairs of buoy positions observed for the period December 3, 1992, to May 20, 1993, are presented in Figure 2 in the form of histograms of the correlation coefficient for artificial shifts, d , from 1 to 5 pixels. It can be seen that the modes of the distributions for $d = 0$ to $d = 2$ are quite similar (close to 0.75) and differ significantly from those for $d \geq 3$. The probability of a correlation >0.75 decreases rapidly as the distance increases and has the values 0.47, 0.36, and 0.24 respectively for $d = 0$ to $d = 2$, respectively. Although these results are encouraging, the quality of the displacements is, in practice, judged by their ability to retrieve the motion and the deformation of a selected ice feature, as described in section 4 of this study.

As an illustration of the results of the method, Plate 2 presents the estimated fields for three consecutive 8-week periods, starting on December 3, 1992, and ending on May 20, 1993, obtained by using the buoys alone (initial displacement field shown on Plate 2a) and after adding scatterometer data (Plate 2b). Displacement fields can be quite different, but the general features of Plate 2 are in good agreement with the mean circulation [Colony and Thorndike, 1984; Serreze et al., 1989], dominated by the transpolar flow and the anticyclonic gyre of the Beaufort Sea. Except in the Fram Strait area, in which the satellite data have been intentionally excluded, and the north pole area, where no satellite data are available because of scatterometer coverage, the average precision of the ice displacement estimation is improved but does not reach the low levels of error variance in the vicinity of the buoys (Plates 2c–2d). In particular, the coastal features of the displacement are more accurately determined when scatterometer data are used. Plate 2c also reveals the poor accuracy of the displacement field derived from the buoys to the north of Novosibirskiye Ostrova during the first two periods studied (from December 3, 1992, to March 25, 1993). The closest buoys, located in the Beaufort Sea and north of Severnaya Zemlya, have displacements relatively small compared to those of the area where our selected ice structure appears (Plate 2a). This explains why during 8-week periods, the estimated ice displacements are increased from one to two pixels (25 to 50 km) when using AMI-Wind data. Although individually small, these improvements summed over a cold season make a significant impact on the automatic tracking of ice features.

4. Formation and Displacement of the Selected Ice Mass

4.1. Formation in July 1992

Cyclones are frequent in summertime and induce divergence, which may decrease the ice concentration [Serreze et al., 1989], mainly in the Canadian Basin, where a maximum of cyclonic activity is generally situated. At the end of July 1992, however, a low-pressure system passed north of Novosibirskiye Ostrova [Colony and Rigor, 1993], pushing ice along the northern shores of the archipelago. From July 24 to August 6, 1992, the evolution of the brightness temperature at 19 GHz (H), Plate 3, shows how quickly the ice pack (characterized by its higher temperatures) was transformed, being broken, melted, and moved away as the cyclone progressed through the area. Deep lows moved east of 180°E, enhancing ice divergence north of Novosibirskiye Ostrova. In summer, σ^0 images cannot

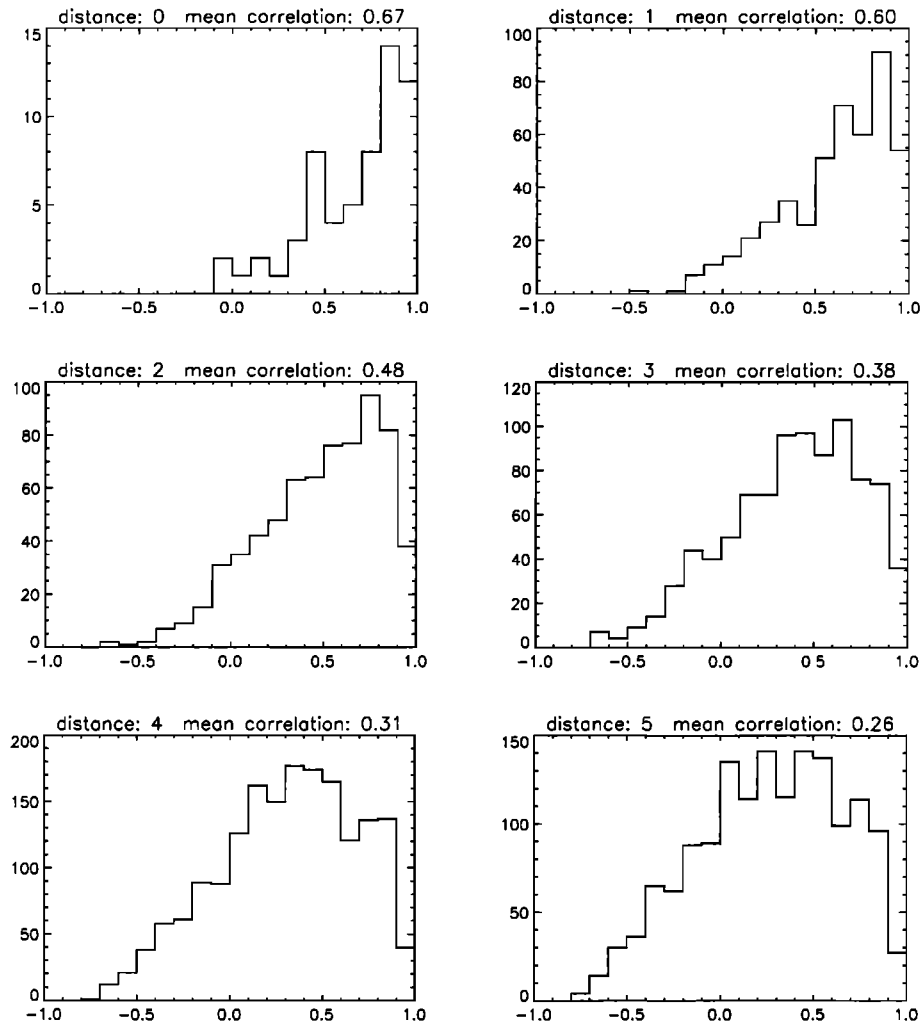


Figure 2. Histograms of correlation coefficients for 7×7 -pixel cell arrays A and B, centered on the positions of buoys 8 weeks apart (distance = 0), and for positions of array B artificially shifted from 1 to 5 pixels (distances from 1 to 5) in any direction.

be used directly because the contrast between open water and ice, covered by melt ponds, is very low. Less sensitive in summer than the backscatter coefficient and better related to ice concentration [Gohin, 1995], images of the derivative of the backscatter, $d\sigma/d\theta$, at 28° incidence angle (Plate 3d) show the same characteristic feature as seen by the SSM/I. Though poorly featured, the ice structure, contoured with a red ellipse on Plates 3c–3d, is already visible at the beginning of August 1992. During August and September, satellite imagery, not shown, confirms this initial situation, which evolves slowly until October (Plates 3e–3h), when the microwave properties are stabilized.

4.2. Locations With Time

From the weekly σ^0 map centered on December 3, 1992, a subimage is manually contoured. This ice area, visible on Plate 4a, is the ice feature selected for this study. It is essentially composed of second-year ice which had just begun drifting away from the Novosibirskiye Ostrova. Using the ice displacement fields previously calculated, the position of each subimage pixel is located on the following backscatter im-

age, and the corresponding subimage is extracted. Plate 4 presents the time series of the ice feature positions as obtained by this method. The quality of the restitution can be estimated by looking at the three first subimages selected from January to May 1993. Although σ^0 evolves, slowly in winter and more quickly in spring, the contours of the selected ice are well retrieved, as well as they could be obtained manually. In November 1993, σ^0 has increased, and the northern part of the feature is hardly discernible from the neighboring ice, while its southern part is quite distinguishable, characterized by high backscatter coefficients (Plate 1e). Ice displacement in the southern part of the feature is less than it is farther in the north. The difference increases with time as the feature is stretched. Three points, indicated on Plate 4a, have been selected on the images, and their displacements, every 8 weeks, are shown on Figure 3. The northern pixel, P1, constantly in the transpolar drift stream, reaches 80°N by August 1994. Its mean displacement is 215 km over 8 weeks, compared to 208 and 154 km for the central and southern pixels, P2 and P3, respectively.

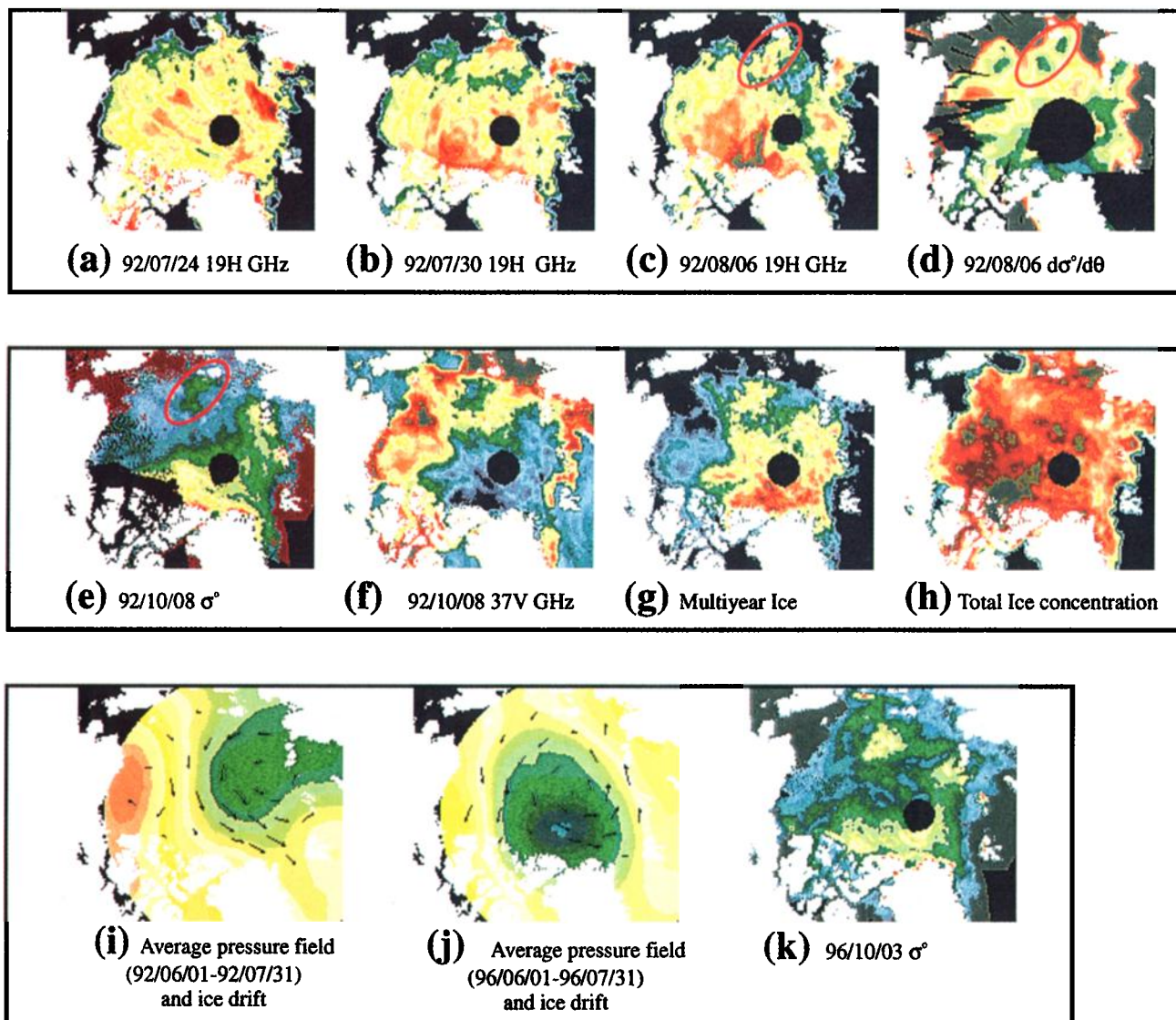


Plate 3. Summer data over the Arctic. (a–c) Images of brightness temperature at 19 GHz (H). (d) The derivative of σ° as a function of the incidence angle confirms the formation of the structure. At the beginning of October, the structure is visible (e) on the image of σ° , as well as (f) on the image of the brightness temperature. The pressure fields averaged over June and July (i) 1992 and (j) 1996, and the displacement fields produced by the International Arctic Buoy Program are shown. The meteorological situation in summer 1996 led to a backscatter distribution in (k) October, similar to that observed in 1992.

5. Evolution of Microwave Signatures and Multiyear Ice Concentration

5.1. Microwave Signatures

An opposite evolution in backscatter coefficient and in brightness temperature is expected [Ezraty *et al.*, 1994], as the parameters are respectively linked to the reflectivity, Γ , and the emissivity, ϵ , which, at a given wavelength and polarization, is

equal to $1 - \Gamma$. However, differences in wavelengths and incidence angles between active and passive microwave measurements generate significant variations.

Generally, the opposite trends expected in active and passive signatures are observed (Plates 3e–3f). However, a maximum in σ° occurs on that part of the ice feature closest to Novosibirskiye Ostrova, while the minimum in brightness temperature is observed farther north. This behavior is also confirmed by the

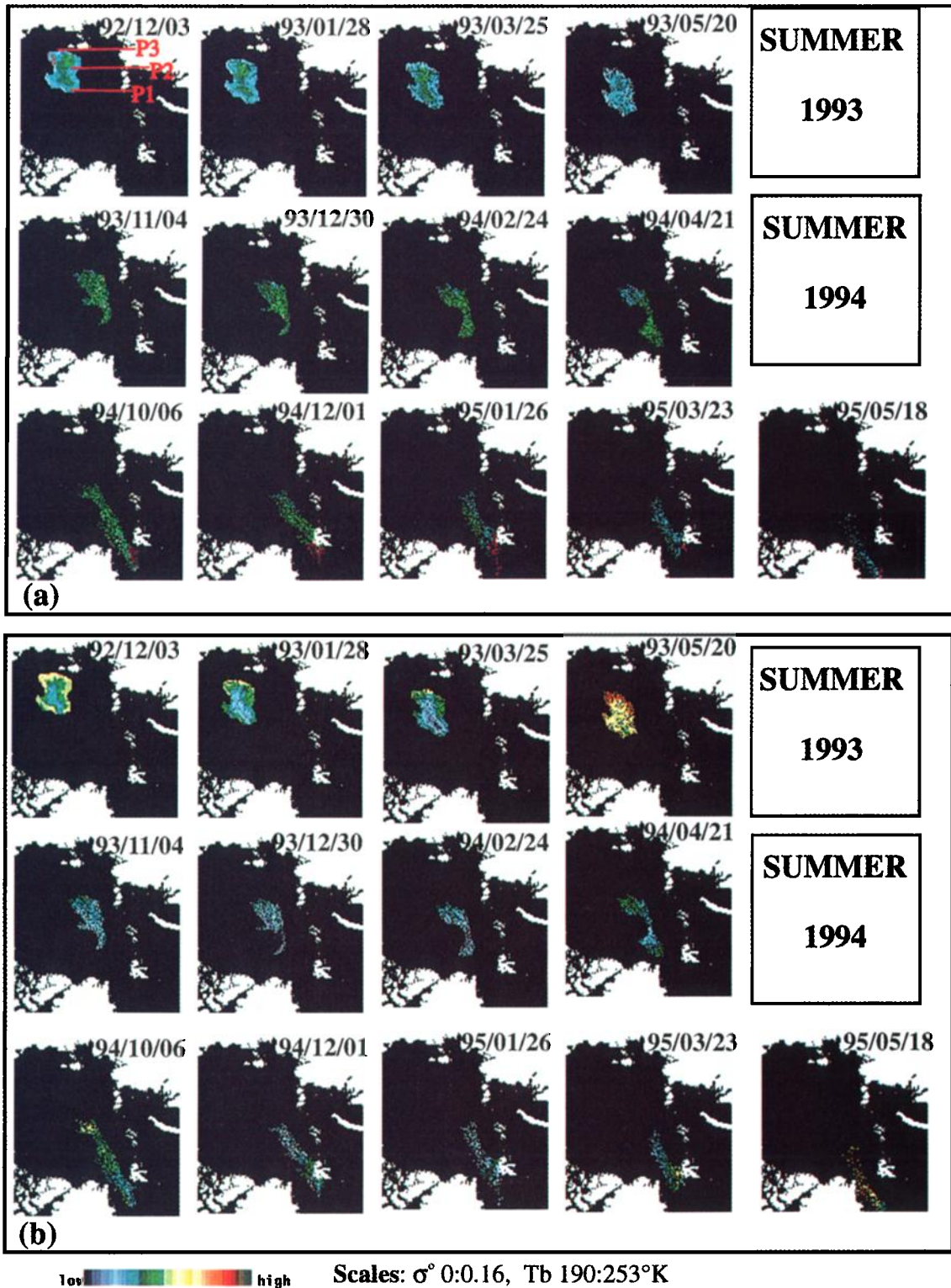


Plate 4. Detail of images along the track of the selected structure; (a) AMI-wind backscatter coefficient and (b) SSM/I brightness temperature at 37 GHz (V).

scatterplot of 37 GHz (V) brightness temperature versus σ^0 on December 3, 1992 (Figure 4d). On Figure 4d the cloud of points splits into two branches; the bottom one, which includes most of the cells of the feature, reaches a minimum in brightness temperature associated to the highest multiyear concentration while the upper one contains the highest values of σ^0 ,

associated with the cells in the vicinity of the coast. The topography of the ice surface there, likely to be rough as the pack has been pushed and compressed to the coast, plays an important role in the σ^0 increase. As expected from previous studies, [Wismann *et al.*, 1996], the time series of σ^0 averaged over the selected feature for a given cold season is much more stable in

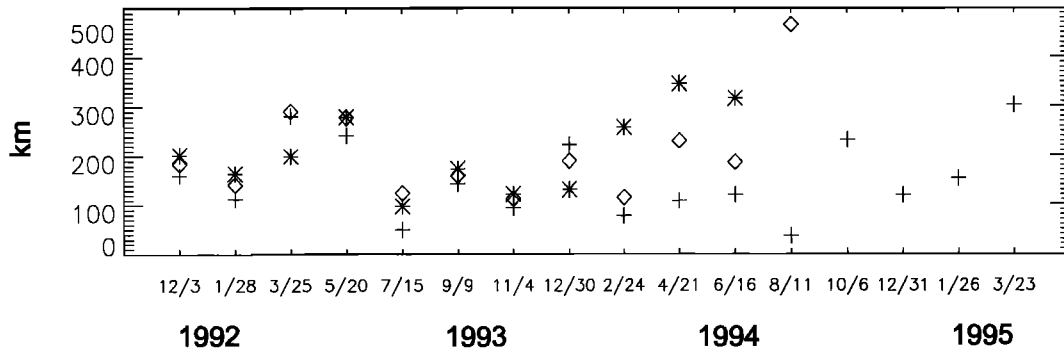


Figure 3. Time series of the estimated displacements over 8-week periods for points P1 (asterisk), P2 (diamond), and P3 (cross). Initial locations are 172°45'E, 82°20'N; 162°25'E, 79°50'N; and 154°E, 75°30'N, respectively.

time than the following passive microwave parameters: brightness temperature, GR, or multiyear ice concentration (Figure 5). This stability in σ^0 is attested not only by the regular level of the averaged backscatter coefficient during the first and the second season but also by the stability of the standard deviation observed on the selected feature (Figure 5b). A small decrease in σ^0 , appearing in spring, coincides with a relatively high increase in brightness temperature and a larger dispersion of

the data. In 1994 the decrease occurs in late April, as shown by the time series of the mean σ^0 ; this is also visible on the corresponding images of Plates 4a–4b.

A significant negative trend in σ^0 occurs only during the third cold season, but by this time the ice feature is exiting through the Fram Strait, and significant divergence, linked to the creation of open water areas, is a reasonable explanation of this evolution. This is confirmed by the clouds of points in the

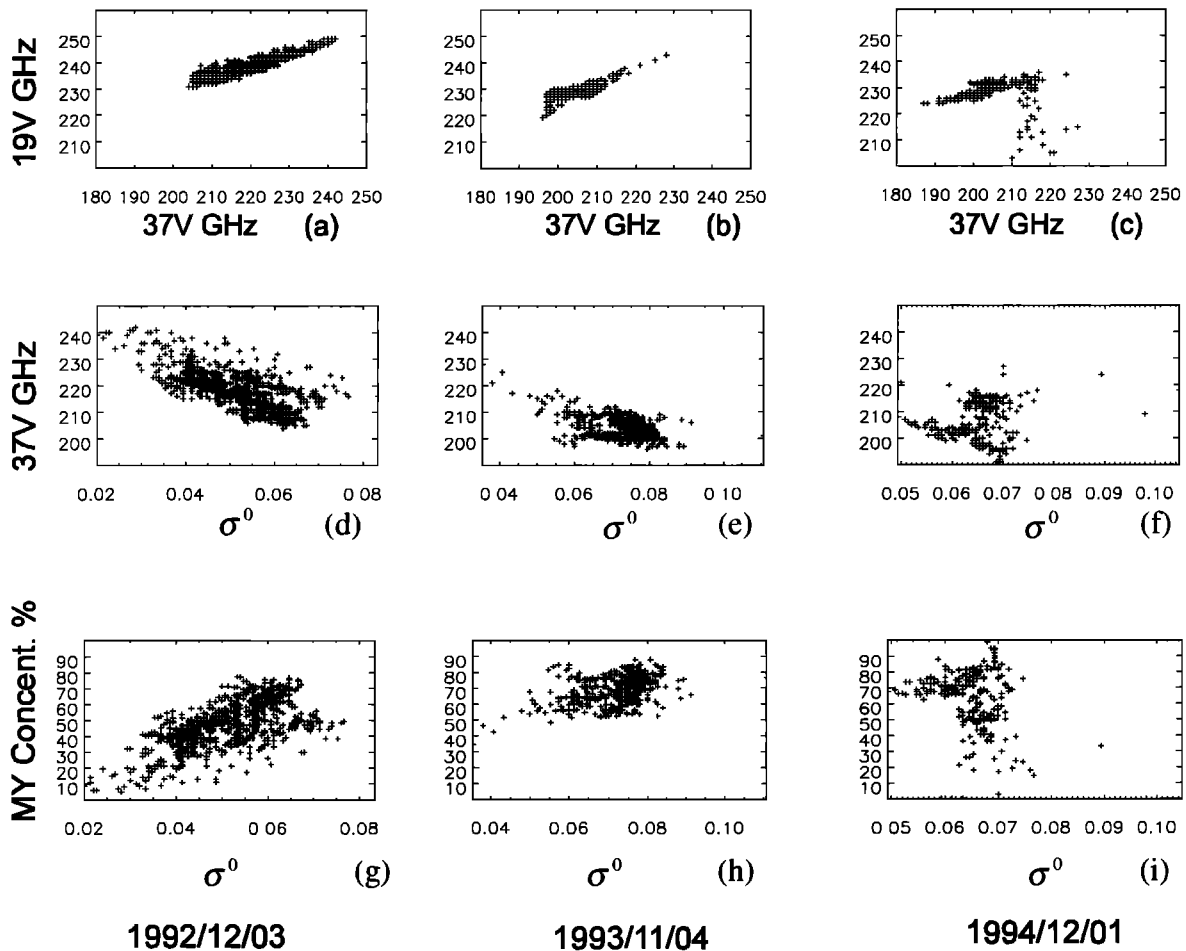


Figure 4. Scatterplots of 19 GHz (V) versus 37 GHz (V), 37 GHz (V) versus σ^0 , and multiyear ice concentration versus σ^0 for the sea ice structure at the beginning of the three cold seasons.

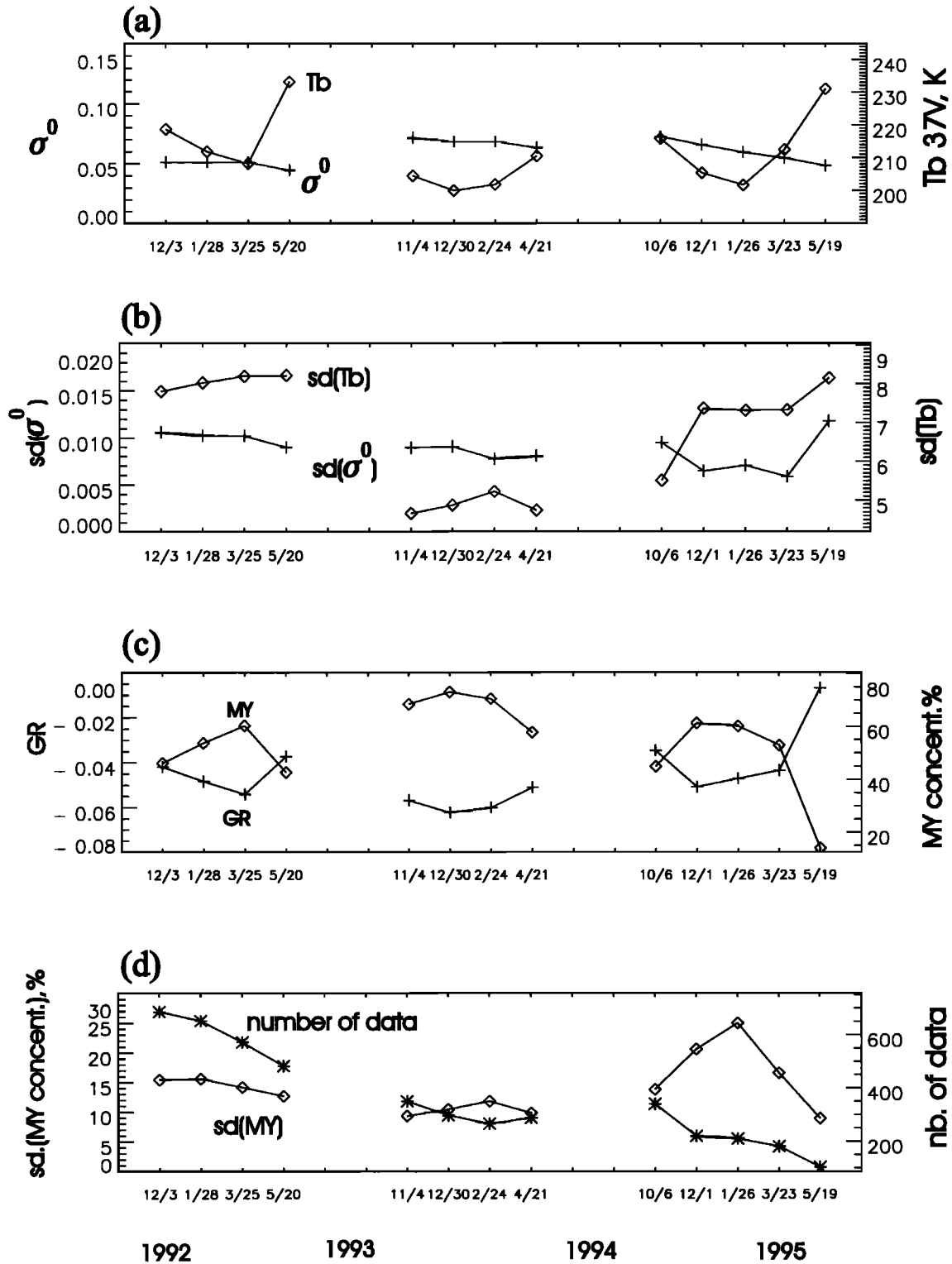


Figure 5. Time evolution of active microwave instrument in wind mode (AMI-wind) backscatter, special sensor microwave imager (SSM/I) brightness temperature and computed parameters over the selected ice structure. (a) Mean backscatter coefficient (cross) and 37-GHz vertically polarized (V) brightness temperature (diamond), (b) standard deviations of backscatter coefficient (cross) and 37-GHz (V) brightness temperature (diamond), (c) gradient ratio (cross) and multiyear ice concentration (diamond), and (d) standard deviation of multiyear ice concentration (diamond) and number of observed ice pixels during the drift (asterisk).

19-GHz (V) versus 37-GHz (V) brightness temperature plots, which depart from the well-known straight line behavior [Comiso, 1986] only during the 1994–1995 winter (Figure 4c).

5.2. Multiyear Ice Concentration

The gradient ratio (Figure 5c) decreased from December 1992 to March 1993 while, inversely, the multiyear ice concentration evolved from 45 to 60%. Because this increase in multiyear ice concentration cannot be justified by advection, it is clearly the result of transformations in the electromagnetic properties of the ice. As noted by Comiso [1990], multiyear ice floes could have first-year ice signatures, especially in zones subject to atmospheric and oceanic forcings; this was the situation encountered in summer 1992 in the area where the ice feature studied was formed. Drainage with time of the saline surface of this second-year ice and the decrease in air temperature due to the displacement toward the north pole and to the seasonal evolution have probably more affected the surface, including the snow cover [Cavalieri *et al.*, 1991] than the interior of the ice. The stability of σ^0 during that period shows that ice is not significantly modified, neither in its surface topography nor in its deeper layers sensed by the scatterometer at C band. As noted previously by several authors in different contexts [Comiso, 1986, 1990; Thomas, 1993; Kwok *et al.*, 1996] but here in a Lagrangian frame, multiyear ice concentrations, as given by the NASA team algorithm, fluctuate considerably in the course of the cold season (Figure 5c). The gradient ratio, far from being constant, is seen to be inversely correlated to the 37-GHz (V) brightness temperature. This important correlation had already been noted but in the context of fixed geographical areas, so that influence of advection could not be eliminated [Wismann *et al.*, 1996].

During the second year of observation, the feature, composed essentially of third-year ice drifting in the vicinity of the north pole, shows a more regular pattern in backscatter and brightness temperature. The multiyear ice concentration is stable and estimated to 75%, which is probably a little low but not unrealistic for third-year ice. The mean level of σ^0 has significantly increased after the summer and stays at a level equivalent to the highest observed during the previous year near the structure. A slow decrease of σ^0 occurs during the third year of observation. This decrease of σ^0 can be attributed to an increase of new ice concentration as ice diverges on approaching the Fram Strait. The multiyear ice concentration reaches 60% in January 1995 before decreasing from March to May, by which time most of the initial structure has passed Fram Strait (Plate 4) and melted or mixed with younger ice.

6. Summary and Conclusion

6.1. Ice Displacement Fields

Over the Arctic Ocean, scattered multiyear ice or contrasted boundaries in σ^0 within second-year ice areas, due to local roughness effects, create contours on backscatter maps that can be utilized for tracking; from year to year, backscatter maps show very different situations, some years being much more favorable for this purpose. Varying atmospheric conditions in summer are crucial as they produce features which will persist through the cold season. In the autumns of 1992 (Plate 3e) and 1996 (Plate 3k), many features of second-year ice appear on the backscatter images. As in 1992, the situation in 1996 can be explained by the atmospheric cyclonic circulation

in summer (Plate 3j), which has modified the usual ice distribution.

To follow the selected ice structure, we have constructed displacement fields of Arctic sea ice based on buoy positions combined with displacements estimated by automatic tracking using successive backscatter maps. Our aim was to follow an identified ice feature and not to provide a general algorithm for estimating the ice displacement over the whole Arctic Ocean in all seasons. For that purpose it would have been absolutely necessary to include wind data [Thorndike and Colony, 1982]. Our procedure is efficient enough to retrieve the ice displacements accurately in the vicinity of buoys and, during the cold season from October to May, at locations where the backscatter maps show high contrasts. This was the case in the vicinity of the ice feature that we selected. The Eulerian displacement fields, applied to the cells of the structure, defined in early December 1992, have allowed a realistic tracking of its displacements, verifiable during the first year.

In the vicinity of the Fram Strait, the method described is ill adapted to study sea ice dynamics because of the rapid sea ice evolution both in space and time. Divergence in this area of accelerated displacements and strong tidal processes on the Yermak Plateau lead to a complex mixing of old, new, and broken first-year ice. In such a region, daily SSM/I 85-GHz brightness temperatures, advanced very high resolution radiometer (AVHRR) observations, when atmospheric conditions are clear, or SAR data [Kergomard *et al.*, 1994; Kornes, 1994] much better describe the situation of the polar pack ice.

6.2. Evolution of Microwave Signatures

The active and passive microwave signatures evolve coherently during the drift of the structure, showing, on average, opposite trends. However, in its earlier stages the backscatter peak is shifted toward the coast, where ice is likely to have been crushed and ridged. During the first cold season the average σ^0 of the structure, which is classified as second-year ice, is constant while the brightness temperatures and the GR show a more erratic behavior; this leads to unrealistic fluctuations in the multiyear ice concentration as evaluated from the NASA team algorithm. We note an increase in multiyear ice concentration from 40 to 65% from December 1992 to March 1993 while convergence seems to be quite limited because of the σ^0 stability. Successive backscatter images show a stretching of the selected ice feature, its northern part drifting slightly faster, in an environment of lower multiyear ice concentration. It is interesting to note that during another cold season and for perennial ice of the Beaufort Sea, Kwok *et al.* [1996] have observed a decrease in the multiyear ice concentration. If the decrease in spring, observed at the end of the cold seasons (May 1993 and April 1994), can be attributed to an increase in atmospheric water vapor, the winter trend is difficult to explain without taking into account a change in emissivity or an effect of the physical temperature as ice is drifting northward.

We agree with the conclusions already published by Thomas [1993] that there are several “types” of multiyear ice, each with its own radiometric signature, itself dependent on the physical temperature which varies spatially. Although there exists a clear relationship between the GR and multiyear ice concentration, it seems to be an impossible task to accurately and coherently estimate the multiyear ice concentration from this parameter alone without taking into account the spatial and temporal continuity of the ice cover from the end of summer to spring.

Acknowledgments. The authors thank the National Snow and Ice Data Center, University of Colorado, for providing the SSM/I data; the Polar Science Center, University of Washington, for the buoy data; and the Centre ERS d'Archivage et de Traitement for processing and providing the AMI-wind backscatter maps. We are particularly grateful to I. G. Rigor (Polar Science Center), who provided the most recent buoy positions available from the IABP. Many comments to the initial draft made by the anonymous reviewers must be acknowledged and have helped to improve the document. This study was partly supported by a 1994 grant of the Programme National de Télédétection Spatiale.

References

- Aagaard, K., and E. C. Carmack, The role of sea ice and other fresh water in Arctic circulation, *J. Geophys. Res.*, **94**(C10), 14,485–14,498, 1989.
- Cavalieri, D. J., Sea ice algorithm, in *NASA Sea Ice Validation Program for the Defense Meteorological Satellite Program Special Microwave Imager: Final Report*, NASA Tech. Memo., 104559, 25–31, 1992.
- Cavalieri, D. J., J. P. Crawford, M. R. Drinkwater, D. T. Eppler, L. D. Farmer, R. R. Jentz, and C. C. Wackerman, Aircraft active and passive microwave validation of sea ice concentration from the Defense Meteorological Satellite Program special sensor microwave imager, *J. Geophys. Res.*, **96**(C12), 21,989–22,008, 1991.
- Colony, R. L., and I. G. Rigor, International Arctic Buoy Program data report for 1 January 1992–31 December 1992, *Tech. Memo. APL-UW TM29-93*, 215 pp., Appl. Phys. Lab., Univ. of Wash., Seattle, 1993.
- Colony, R., and A. S. Thorndike, An estimate of the mean field of the Arctic sea ice motion, *J. Geophys. Res.*, **89**(C6), 10,623–10,629, 1984.
- Comiso, J. C., Characteristics of Arctic winter sea ice from satellite multispectral microwave observations, *J. Geophys. Res.*, **91**(C1), 975–994, 1986.
- Comiso, J. C., Arctic multiyear ice classification and summer ice cover using passive microwave satellite data, *J. Geophys. Res.*, **95**(C8), 13,411–13,422, 1990.
- Curran, P. J., The semi-variogram in remote sensing, An introduction, *Remote Sens. Environ.*, **24**, 493–507, 1988.
- Dickson, R. R., J. Meincke, S.-A. Malmberg, and A. J. Lee, The 'Great Salinity Anomaly' in the northern North Atlantic 1968–1982, *Prog. Oceanogr.*, **20**, 103–151, 1988.
- Drinkwater, M. R., and F. D. Carsey, Observations of the late-summer to fall sea ice transition with the 14.6 GHz Seasat scatterometer, in *Proceedings of IGARSS'91, Helsinki, Finland*, vol. 3, pp. 1597–1600, Inst. of Electr. and Electron. Eng. Geosci. and Remote Sens. Soc., Spring, Tex., 1991.
- Ezraty, R., F. Gohin, and A. Cavanié, Arctic sea ice during the winter to summer transition as seen by the AMI-Wind and ATSR/M of ERS-1, *EARSeL Adv. Remote Sens.*, **3**, 100–111, 1994.
- Fily, M., and D. A. Rothrock, Sea ice tracking by nested correlations, *IEEE Trans. Geosci. Remote Sens.*, **GE-25**(5), 570–580, 1987.
- Gloersen, P., Modulation of hemispheric sea-ice cover by ENSO events, *Nature*, **373**, 503–506, 1995.
- Gloersen, P., W. J. Campbell, D. J. Cavalieri, J. Comiso, C. L. Parkinson, and H. J. Zwally, Arctic and Antarctic sea-ice, 1978–1987: Satellite passive-microwave observations and analysis, *NASA Spec. Publ.*, NASA SP-511, 290 pp., 1992.
- Gohin, F., Some active and passive microwave signatures of Antarctica sea ice from mid-winter to spring 1991, *Int. J. Remote Sens.*, **16**, 2031–2054, 1995.
- Gohin, F., and A. Cavanié, A first try at identification of sea ice using the three beam scatterometer of ERS-1, *Int. J. Remote Sens.*, **15**, 1221–1228, 1994.
- Häkkinen, S., An Arctic source for the Great Salinity Anomaly: A simulation of the Arctic ice-ocean system for 1955–1975, *J. Geophys. Res.*, **98**(C9), 16,397–16,410, 1993.
- Haverkamp, D., L. K. Soh, and C. Tsatsoulis, A comprehensive, automated approach to determining sea ice thickness from SAR data, *IEEE Trans. Geosci. Remote Sens.*, **33**(1), 46–57, 1995.
- Kergomard, C., J. C. Gascard, M. Fily, C. Delacourt, C. Lefort, and D. Darr, The transpolar ice drift north of Fram Strait studied from ERS-1 SAR imagery, in *Proceedings of the Second ERS-1 Symposium—Space at the Service of Our Environment*, Eur. Space Agency Spec. Publ., SP-361, 263–267, 1994.
- Kornes, R., An ice drift series from the Fram Strait January–March 1992 based on ERS-1 SAR data, *Polar Res.*, **13**(1), 55–58, 1994.
- Kwok, D., A. Rothrock, H. L. Stern, and G. F. Cunningham, Determination of the age distributions of ice motion, *IEEE Trans. Geosci. Remote Sens.*, **33**(2), 392–400, 1995.
- Kwok, D., J. C. Comiso, and G. F. Cunningham, Seasonal characteristics of the perennial ice cover of the Beaufort Sea, *J. Geophys. Res.*, **101**(C12), 28,417–28,439, 1996.
- Matheron, G., La théorie des variables généralisées et ses applications; Ecole Nationale Supérieure des Mines de Paris, *Cah. Cent. Morphol. Math. Fontainebleau*, **5**, 1–212, 1970.
- Olea, R. A., Optimal contour mapping using universal kriging, *J. Geophys. Res.*, **79**(5), 695–701, 1974.
- Serreze, M. C., R. G. Barby, and A. S. McLaren, Seasonal variations in sea ice motion and effects on sea ice concentration in the Canadian Basin, *J. Geophys. Res.*, **94**(C8), 10,955–10,970, 1989.
- Steffen, K., J. Key, J. Cavalieri, J. Comiso, P. Gloersen, K. St. Germain, and I. Rubinstein, The estimation of geophysical parameters using passive microwave algorithms, in *Microwave Remote Sensing of Sea Ice*, *Geophys. Monogr. Ser.*, vol. 68, edited by F. D. Carsey, pp. 201–231, AGU, Washington, D. C., 1992.
- Thomas, D. R., Arctic Sea ice signatures for passive microwave radiometry, *J. Geophys. Res.*, **98**(C6), 10,037–10,052, 1993.
- Thorndike, A. S., and R. Colony, Sea ice motion in response to geostrophic winds, *J. Geophys. Res.*, **87**(C8), 5845–5852, 1982.
- Walsh, J. E., and H. J. Zwally, Multiyear sea ice in the Arctic: Model- and satellite-derived, *J. Geophys. Res.*, **95**(C7), 11,613–11,628, 1990.
- Wismann, V., K. Boehnke, A. Cavanié, R. Ezraty, F. Gohin, D. Hoekman, and I. Woodhouse, Land surface observations using the ERS-1 windscatterometer, II, report, contract 11103/94/NL/CN, Eur. Space Agency, Paris, 1996.

A. Cavanié, R. Ezraty, and F. Gohin, IFREMER, Centre de Brest, BP 70 29280 Plouzané, Breizh, France. (e-mail: gohin@ifremer.fr)

(Received January 29, 1997; revised November 2, 1997; accepted November 10, 1997.)